Interannual sea-air CO2 flux variability from an observation-driven ocean mixed-layer scheme

Christian Rödenbeck, Dorothee C. E. Bakker, Nicolas Metzl, Are Olsen, Christopher L. Sabine, Nicolas Cassar, F. Reum, Ralph F. Keeling, M. Heimann

Biogeosciences Discuss., 11, 3167–3207, 2014
www.biogeosciences-discuss.net/11/3167/2014/
doi:10.5194/bgd-11-3167-2014

Biogeosciences Discussions
Open Access

Interannual sea–air CO_2 flux variability from an observation-driven ocean mixed-layer scheme

C. Rödenbeck[1], D. C. E. Bakker[2], N. Metzl[3], A. Olsen[4,5], C. Sabine[6], N. Cassar[7], F. Reum[1], R. F. Keeling[8], and M. Heimann[1]

[1]Max Planck Institute for Biogeochemistry, Jena, Germany
[2]School of Environmental Sciences, University of East Anglia, Norwich Research Park, Norwich, UK
[3]LOCEAN-IPSL, CNRS, Paris, France
[4]Geophysical Institute, University of Bergen and Bjerknes Centre for Climate Research, Bergen, Norway
[5]Uni Climate, Uni Research AS and Bjerknes Centre for Climate Research, Bergen, Norway
[6]NOAA Pacific Marine Environmental Laboratory, Seattle, USA
[7]Division of Earth and Ocean Sciences, Duke University, Durham, USA
[8]Scripps Institution of Oceanography, University of California, San Diego, USA

Received: 20 January 2014 – Accepted: 13 February 2014 – Published: 25 February 2014

Correspondence to: C. Rödenbeck (christian.roedenbeck@bgc-jena.mpg.de)

Published by Copernicus Publications on behalf of the European Geosciences Union.

Abstract

Interannual anomalies in the sea–air carbon dioxide (CO_2) exchange have been estimated from surface-ocean CO_2 partial pressure measurements. Available data are sufficient to constrain these anomalies in large parts of the tropical and Northern Pacific and in the Northern Atlantic, in some areas since the mid 1980s to 2011. Global interannual variability is estimated as about 0.31 Pg C yr^{-1} (temporal standard deviation 1993–2008). The tropical Pacific accounts for a large fraction of this global variability, closely tied to ENSO. Anomalies occur more than 6 months later in the East than in the West. The estimated amplitude and ENSO response are consistent with independent information from atmospheric oxygen data. Despite discrepancies in detail, this both supports the variability estimated from surface-ocean carbon data, and demonstrates the potential of the atmospheric oxygen signal to constrain ocean biogeochemical processes. The ocean variability estimated from surface-ocean carbon data can be used to improve land CO_2 flux estimates from atmospheric inversions.

1 Introduction

The ocean currently accounts for about half the sink of excess atmospheric CO_2 (Sarmiento et al., 2010). Long-term changes in this sink capacity therefore affect the climate change trajectory. In order to be able to relate changes in sea–air CO_2 exchanges to driving influences and to test concepts or models, contemporary variations need to be quantified from suitable data sets.

In a previous study (Rödenbeck et al., 2013), the spatio-temporal variability of sea–air CO_2 fluxes has been estimated based on the SOCAT data base (Surface Ocean CO_2 Atlas v1.5, Pfeil et al., 2013) of surface-ocean CO_2 partial pressure measurements, using a diagnostic data-driven scheme of mixed-layer biogeochemistry. That study focused on seasonal variations, which were found to be well constrained from the data in most parts of the ocean. Estimated mean seasonal cycles are similar to

BGD
11, 3167–3207, 2014

the seminal climatology by Takahashi et al. (2009). In addition, the scheme also reproduces part of day-to-day variations through parametrizations in terms of sea surface temperature and a few other variables. Using phosphate observations, plausibility of the scheme was tentatively confirmed on the seasonal time scale.

As a next step, we now also consider interannual variations (IAV). In particular, we consider the following questions:

- What are the main modes of interannual variability contributing to the global sea–air CO_2 flux?
- Not all parts of the ocean have been sampled frequently enough to reliably estimate interannual flux variations from the SOCAT data. In which parts of the ocean, and to which extent, does the available data coverage suffice to estimate interannual variations of the sea–air CO_2 flux?
- The ocean-internal processes (biology, transport) that add/remove dissolved inorganic carbon to/from the mixed-layer and thus cause anomalies in sea–air CO_2 fluxes, simultaneously also remove/add dissolved oxygen, leading to anomalies in the sea–air oxygen exchange and finally to tiny but detectable variations in the atmospheric oxygen abundance. Thus, regular atmospheric oxygen measurements contain information on ocean-internal biogeochemical processes (Keeling and Shertz, 1992). Using an atmospheric inversion technique, the atmospheric oxygen (and CO_2) observations at 5 sites operated since at least 1993 have been shown to be more or less sufficient to estimate interannual variations of the oceanic oxygen flux independently for at least 3 latitudinal bands (Rödenbeck et al., 2008). As the data-driven diagnostic mixed-layer scheme used here can be extended to calculate sea–air oxygen fluxes as well (by exploiting the above-mentioned link between the ocean-internal sources and sinks of carbon and oxygen), we can compare the SOCAT-based variations to those based on atmospheric oxygen. How consistent are these independent information sources?

BGD
11, 3167–3207, 2014

We further compare the SOCAT-based estimates to ocean process model results, and discuss the estimates in the context of atmospheric CO_2 inversions.

2 Method

2.1 The data-driven mixed-layer scheme

This paper further analyzes the spatio-temporal fields of surface-ocean CO_2 partial pressure (pCO_2) and sea–air CO_2 flux presented in the companion paper Rödenbeck et al. (2013) (run SFC). As documented in detail there, these fields were estimated by fitting a simple diagnostic model of mixed-layer biogeochemistry to SOCAT pCO_2 data in the following way: (1) A mixed-layer carbon budget equation (including simple parameterizations of sea–air CO_2 exchange (Wanninkhof, 1992), solubility (Weiss, 1974), and carbonate chemistry (Sarmiento and Gruber, 2006), driven by observation-based environmental fields listed in Table 1) was used to express surface-ocean pCO_2 and sea–air CO_2 flux as a function of ocean-internal carbon sources and sinks (Fig. 1) for each pixel. (2) A cost function was formed to measure the mismatch between the individual pCO_2 data points in SOCAT and the model's pCO_2 field at the corresponding location and time. (3) The ocean-internal carbon sources and sinks were adjusted as to minimize this model-data mismatch. In order to interpolate areas/periods without data, additional smoothness constraints were applied (similar to those in the atmospheric inversion of Rödenbeck, 2005). The only difference of the present estimates with respect to Rödenbeck et al. (2013) is that we updated the data source to the ship-board observations[1] of SOCAT v2 (Pfeil et al., 2013; Bakker et al., 2013) offering data coverage until end of 2011.

[1]The high-frequency mooring and drifter observations available in recent years have been retained for independent validation (Sect. S3.2). This also provides a more uniform data density throughout time.

BGD
11, 3167–3207, 2014

The calculation has been done on a global grid of $\approx 4^{\circ} \times 5^{\circ}$ pixels and daily time steps over 1985–2012 (inclusive). The first and last year will be discarded from any plots to avoid edge effects. Statistical analysis is done over 1993–2008 (inclusive) only, as this is a period with largest data coverage both in SOCAT v2 and in atmospheric oxygen records. To obtain interannual variations, we de-seasonalize the time series by subtracting the mean seasonal cycle (1993–2008) and remove variations faster than about 1 year by a spectral filter corresponding to a Gaussian smoothing kernel (Rödenbeck, 2005).

2.2 Process contributions to variability

For any given location, the (interannual) variability of the sea–air CO_2 flux is the sum of two contributions:

Contribution OIS (Ocean-Interior Sources/sinks). Variations in biological conversion and/or ocean transport into the mixed layer lead to anomalous ocean-internal sources/sinks $f_{\mathrm{int}}^{\mathrm{DIC}}$ of dissolved inorganic carbon (DIC) (Fig. 1 bottom), which then lead to enhanced/reduced sea–air CO_2 fluxes $f_{\mathrm{ma}}^{\mathrm{CO_2}}$ (Fig. 1 top). The responses in $f_{\mathrm{ma}}^{\mathrm{CO_2}}$ are however of smaller magnitude than and delayed with respect to the causes in $f_{\mathrm{int}}^{\mathrm{DIC}}$, because the buffering capacity of carbonate chemistry (Revelle factor) strongly enhances the limiting effect of the finite gas exchange velocity.

Contribution TE (Thermally induced Exchange). Even in the absence of ocean-internal sources or sinks, the sea–air flux varies in response to temperature-induced changes in solubility and chemical equilibrium[2] (plus minor contributions from changes in atmo-

[2] Though contribution TE is mainly driven by the "thermal component of pCO_2" considered in the literature (Takahashi et al., 2009), its temporal course differs from that of SST, because besides the static dependence of pCO_2 on temperature it also takes into account the dynamic response of the mixed-layer DIC content: temperature rise(decline) induces out(in)gassing fluxes

BGD
11, 3167–3207, 2014

spheric pressure, freshwater effects, and alkalinity). Contribution TE also comprises a secular CO_2 uptake (and consequent rise of pCO_2) induced by the prescribed rising atmospheric CO_2 content.

Both contributions are somewhat modulated by variations in gas exchange (Supplement, Sect. S5) and mixed-layer depth.

In the diagnostic scheme, contribution TE is considered known from the employed process parametrizations driven by observed variables (predominantly Sea Surface Temperature (SST)). In contrast, the ocean-internal DIC sources/sinks $f_{\mathrm{int}}^{\mathrm{DIC}}$ causing contribution OIS are taken as unknowns, to be adjusted in such a way that the total variations in the CO_2 partial pressure (sum of contributions OIS and TE) are compatible with the SOCAT data (for illustration see also Fig. 3 of Rödenbeck et al., 2013). The Bayesian prior is chosen to be $f_{\mathrm{int}}^{\mathrm{DIC}} = 0$, such that any positive or negative anomalies in the ocean-internal sources/sinks are a-priori equally likely, i.e., we do not assume any prior knowledge on the ocean-internal processes. Consequently, the prior of the sea–air flux coincides with contribution TE.

2.3 Performance diagnostics

2.3.1 Reduction of uncertainty (RoU)

As the main diagnostic to identify which regions are well constrained by the data, we use the "reduction of uncertainty" (RoU), a standard diagnostic of Bayesian estimation defined as

$$\mathrm{RoU} = 1 - \frac{\sigma_{\mathrm{post}}}{\sigma_{\mathrm{pri}}} \tag{1}$$

which counteract the direct temperature effect. As a consequence of this balance, peaks in the TE contribution tend to be related to temperature *changes* and thus occur earlier than the actual temperature peaks.

BGD
11, 3167–3207, 2014

with σ_{pri} and σ_{post} denoting the formal a-priori and a-posteriori uncertainties of the flux. High values (RoU towards 1) indicate strong data constraints, while low values (close to 0) indicate that the data are not able to move the estimates away from the prior.

The uncertainty intervals σ_{pri} and σ_{post} have been calculated statistically from an ensemble of $n = 50$ inversion runs with pseudo-random realizations of a-priori errors and model-data mismatch errors (drawn according to their specified uncertainties). Each member i of the pseudo-random ensemble gives a realization $\Delta_i f_{post}$ of the a-posteriori error of the flux field. The uncertainties σ_{pri} and σ_{post} are then given by the root mean square of the error fields across the ensemble, $\sigma = \sqrt{\sum_i (\Delta_i f)^2 / n}$ (as the expectation value of the error is zero by construction). As we want to obtain RoU specifically for interannual variations (and possibly for regional averages), the a-priori and a-posteriori error fields of each ensemble member are interannually filtered (and regionally averaged) in the same way as the actual flux estimates, before the root mean square is calculated. That way, any covariances between the a-posteriori errors at different locations/times are automatically taken into account.

Of course, the root mean square across the finite ensemble only gives an approximation to the uncertainty intervals. For our sample size of 50, standard deviations could be a factor 0.79 smaller or a factor 1.34 larger (confidence interval for a confidence level of 99 %). Calculated RoU values can therefore only give the 1st order pattern of the strength of the data constraint. When calculating the overall performance over a given time period, however, we increased the sample size (and thus improved the statistics) by calculating the root mean square error not only across the ensemble but also across all monthly values of the flux error realizations within that period (method proposed by Chevallier et al., 2007).

2.3.2 Test of independence from IAV in the drivers

Most driving variables of the mixed-layer scheme (in particular SST) also contain interannual variations. If a region is well-constrained with respect to IAV, however, then the

BGD
11, 3167–3207, 2014

IAV of the estimated pCO_2 field should only depend on the signals in the pCO_2 data, "overwriting" any influence of IAV in the drivers. We thus performed a test run in which any IAV has been removed from the driver variables (except for a linear rising trend in atmospheric CO_2). In well-constrained regions the result will be similar to the standard result. We use this as a qualitative confirmation to the RoU diagnostic.

Remark: for quantities other than the pCO_2 field, IAV in the drivers can of course be important also in well-constrained regions, for example IAV in wind speed influencing sea–air CO_2 fluxes.

2.3.3 Synthetic data test

Another traditional method to assess the strength of the data constraint (also used in Rödenbeck et al., 2013, for seasonality) is "synthetic data tests" where (1) a modelled pCO_2 field is sampled at the locations/times of the SOCAT data to create a synthetic data set, and (2) a pCO_2 field is retrieved by the diagnostic mixed-layer scheme from the synthetic data and compared to the original modelled field as the known "true" answer. However, this method is dependent on the particular time course of the chosen synthetic "truth", confounding any information about the temporal changes in the strength of the constraint. Despite the higher computational demand, we therefore prefer the RoU diagnostic (Sect. 2.3.1) here. Nevertheless, synthetic data tests have been performed to check consistency with the RoU diagnostic (not shown).

2.3.4 Sensitivity tests

In addition to gaps in data coverage, results may be affected by uncertainties in parameters or input data sets used in the calculation. To assess these errors, we performed a series of sensitivity runs varying those parameters that are considered most uncertain: (i) increase and decrease of the a-priori uncertainty by a factor 2, leaving more/less freedom to inverse adjustments, (ii) decrease of the a-priori uncertainty of non-seasonal variations in $f_{\mathrm{int}}^{\mathrm{DIC}}$ by a factor 2, (iii) decrease in the spatial correlation

BGD
11, 3167–3207, 2014

lengths in latitude direction by a factor 2, (iv) increase and decrease of the global mean piston velocity by 3.2 cm h^{-1} (range given by Naegler, 2009), or using a cubic dependence of piston velocity on wind speed (still keeping the global mean piston velocity at the value from Naegler, 2009), (v) increase and decrease of the mixed-layer depth h by a factor 2. As all these changes are still considered reasonable values, the envelope of these sensitivity results (range between smallest and largest value at each time) gives a lower bound of the error (to be plotted as grey bands).

2.3.5 Residuals and comparison to independent time series

As a consistency check of the fit, residuals between the estimated pCO_2 field and the SOCAT data are assessed. According to the Supplement (Sect. S3.1), the data are fit within 10 to 15 µatm (root-mean-squared residuals), consistent with assumed mismatch uncertainty. Any remaining interannual signals in the residuals are negligible, confirming that the data information is used completely.

Short-term variations are further validated against high-frequency time series from various moorings not used in the fit (Supplement, Sect. S3.2). For testing interannual variations, independent continuous long-term surface-ocean carbon time series are used (Supplement, Sect. S3.3).

2.4 Lagged correlation analysis

To assess the relation of estimated interannual flux anomalies to ENSO, we correlate them to the Multivariate El Niño Index (MEI) by Wolter and Timlin (1993). MEI has been interannually filtered in the same way as the flux (Sect. 2.1). The correlation is calculated for different time lags between flux and MEI; we always report the maximum correlation coefficient. If local maxima exist for several lags, we chose the smallest absolute lag.

BGD
11, 3167–3207, 2014

Correlations have been calculated over the 1993–2008 analysis period. Assuming each of these 16 years to be statistically independent, correlations are moderately significant (at the 90 % level) if their correlation coefficient exceeds 0.50.

2.5 Calculating sea–air oxygen fluxes

In order to relate the SOCAT-based variability estimates to inverse estimates by Rödenbeck et al. (2008) based on atmospheric oxygen data, we extend the diagnostic mixed-layer scheme in three steps:

2.5.1 Ocean-internal oxygen sources/sinks

The ocean-internal processes (biology, transport) that add or remove dissolved inorganic carbon to/from the mixed-layer also add or remove dissolved oxygen (symbolized as box "TT" in Fig. 2). Biological respiration/photosynthesis lead to opposite, mutually proportional changes in carbon and oxygen that we assume to follow a fixed Redfield stoichiometry. Mixing of water from the ocean interior into the mixed layer can change its carbon and oxygen concentrations as well. These transport-induced changes do not follow a simple stoichiometry, but analysis of vertical tracer gradients suggests that their mutual relation is also roughly in Redfield proportions. We therefore assume

$$f_{\mathrm{int}}^{\mathrm{O_2}} = r_{\mathrm{O_2:C}} \cdot f_{\mathrm{int}}^{\mathrm{DIC}} \tag{2}$$

with the Redfield ratio $r_{\mathrm{O_2:C}} = -150/106 \approx -1.4$ (Anderson, 1995) as an approximation.

2.5.2 Sea–air oxygen fluxes

Sea–air oxygen fluxes $f_{\mathrm{ma}}^{\mathrm{O_2}}$ are calculated from $f_{\mathrm{int}}^{\mathrm{O_2}}$ (Eq. 2) using parameterizations of the mixed-layer oxygen budget and sea–air oxygen exchange (Fig. 2, middle column). These oxygen parameterizations are analogous to those of carbon (left column) detailed in Rödenbeck et al. (2013), except that (i) different coefficients are used in the

BGD
11, 3167–3207, 2014

calculation of solubility and Schmidt number (see Supplement of Rödenbeck et al., 2013), (ii) there is no equivalent to carbonate chemistry involved, (iii) sea–air oxygen exchange contains an additional contribution from air injection through bubbles[3].

2.5.3 Atmospheric Potential Oxygen (APO) fluxes

The use of atmospheric oxygen data involves the complication that the atmospheric oxygen abundance is also influenced by oxygen exchanges from the land biosphere. To account for that, the inversion (Rödenbeck et al., 2008) has not been applied to oxygen

[3]Gas injection by bubbles is parametrized by

$$f_{\mathrm{bubb}}^{\mathrm{O_2}} = X^{\mathrm{O_2}} \cdot f_{\mathrm{bubb}}^{\mathrm{Air}} \tag{3}$$

with the oxygen mixing ratio $X^{\mathrm{O_2}} = 209\,392$ ppm. This assumes complete dissolution of bubbles (shown to be the dominating process, Stanley et al., 2009). The air injection flux (positive for injection into the ocean) is taken to depend on wind speed u according to (Monahan and Torgersen, 1990)

$$f_{\mathrm{bubb}}^{\mathrm{Air}} = \begin{cases} B(u-u_0)^3 \frac{p_{\mathrm{baro}}}{R_{\mathrm{gas}}(T+T_0)}, & u > u_0 \\ 0, & \text{else} \end{cases} \tag{4}$$

with the threshold wind speed $u_0 = 2.27\,\mathrm{m\,s^{-1}}$, barometric pressure p_{baro}, gas constant $R_{\mathrm{gas}} = 8.3144\,\mathrm{J\,mol^{-1}\,K^{-1}}$, and absolute temperature $T + T_0$. The global constant B has been calculated such that the global diffusive gas exchange $f_{\mathrm{ge}}^{\mathrm{O_2}}$ calculated from the World Ocean Atlas (WOA) climatology of surface-ocean dissolved oxygen (Garcia et al., 2006) equals the global bubble injection flux, such that the long-term global sea–air oxygen flux is zero.

It should be noted that the bubble flux has only very little influence on the sea–air oxygen fluxes fluxes calculated here from internal O_2 sources and sinks: due to the fast equilibration of dissolved oxygen with the atmosphere (within less than a month), the oxygen input by bubbles is essentially compensated (on interannual time scales) by a corresponding enhancement in the diffusive sea–air oxygen exchange.

BGD
11, 3167–3207, 2014

itself but to the conceptual tracer "Atmospheric Potential Oxygen" (APO) introduced by Stephens et al. (1998). APO is defined as a combination of O_2 and CO_2 abundances in such a way that its surface-to-atmosphere fluxes are

$$f^{\mathrm{APO}} = f^{\mathrm{O_2}} + 1.1 \cdot f^{\mathrm{CO_2}} \quad (5)$$

As O_2 exchanges from the land biosphere are, to good approximation, −1.1 times the CO_2 exchanges, they cancel each other in the APO flux. There is a remaining contribution from fossil fuel burning as it has a slightly different stoichiometry (about −1.4, Keeling, 1988), but this contribution has been accounted for in the APO inversion based on fuel-use statistics (see Rödenbeck et al., 2008). Thus, the APO inversion yields an estimate of the oceanic APO flux $f_{\mathrm{ma}}^{\mathrm{APO}}$.

The comparison is therefore done in terms of $f_{\mathrm{ma}}^{\mathrm{APO}}$. The SOCAT-based APO flux has been calculated according to Eq. (5) from the (dominant) oxygen contribution $f_{\mathrm{ma}}^{\mathrm{O_2}}$ obtained as described above, and the (small) carbon contribution $f_{\mathrm{ma}}^{\mathrm{CO_2}}$ directly available from the *SFC* calculation. The atmospheric inversion of Rödenbeck et al. (2008) has been updated by adding more recent observations to extend the time period to end of 2011.

3 Results and discussion

3.1 Overview

While the sea–air CO_2 flux varies on interannual, seasonal, and day-to-day time scales (Fig. 3, top), this paper focuses on interannual anomalies of the sea–air CO_2 flux around its mean (filtered flux, bottom). The largest contributions to the global interannual variability (IAV) are estimated to come from the subpolar North Pacific and Atlantic, the tropical Pacific, and parts of the Southern Ocean (Fig. 4, top). Due to its large size and its spatially coherent variations, the tropical Pacific (15° S–15° N) provides the largest contribution (Fig. 5, top), with a temporal standard deviation of about

BGD
11, 3167–3207, 2014

40 % of that of the global ocean[4]. Consistent with the literature (e.g., Feely et al., 1999; Inoue et al., 2001; Feely et al., 2002), the sea–air CO_2 flux anomalies are strongly tied to El Niño/Southern Oscillation (ENSO), with a reduced CO_2 source during El Niño phases (see Sect. 3.4 below).

3.2 Strength of the data constraint on IAV

To identify which parts of the ocean have been sampled frequently enough to reliably estimate interannual flux variations from the SOCAT data, Fig. 4 (bottom) shows the "reduction of uncertainty" (RoU) defined in Sect. 2.3.1. It indicates the strength of the data to detect deviations of the flux from its climatological mean. Good constraints (larger RoU) are found in the tropical and Northern Pacific and in the North Atlantic, highlighting the large long-running observational programs by US, Japanese, and European research groups. Specifically, the locations of the repeated cruises crossing the Equator are seen, as well as the ship routes traversing the North Atlantic. In contrast, poor constraints (low RoU, even below the arbitrary threshold of 0.2 left uncolored in the map) prevail in the Indian Ocean and most parts of the Southern-hemisphere extratropical Ocean.

Figure 4 (bottom) gives the overall performance within 1993–2008. Depending on the region considered, this period may comprise both well constrained and badly constrained years (Fig. S1). For example, the RoU in the extratropical North Atlantic clearly increased after the implementation of the pCO_2 observing network in the first half of the 2000s (Watson et al., 2009) and has remained steady at between approximately 0.6 and 0.8 since then.

In well-constrained regions/periods (high RoU), estimated interannual anomalies are essentially independent of the prior. For example, the data are able to almost reverse the a-priori anomalies in the tropical Pacific (Fig. 5). Strong constraints in the tropical

[4]Over 1993–2008, the global standard deviation is about 0.31 Pg C yr^{-1}, that of the tropical Pacific 0.13 Pg C yr^{-1}.

BGD
11, 3167–3207, 2014

Pacific are further confirmed by a test run without interannual variations in all driving variables (Sect. 2.3.2): despite the corresponding substantial change in the prior, the estimated pCO_2 anomalies hardly change (not shown). In contrast, poorly constrained regions (low RoU) stay close to the prior (Fig. S1). In areas where the temperature-related variability (contribution TE contained in the prior, Sect. 2.2) dominates IAV, the results of the diagnostic mixed-layer scheme may still capture part of the real IAV, otherwise the variability from the ocean-internal fluxes (contribution OIS) is missing there.

The pattern of RoU shown in Fig. 4 is similar to the map of number of data points (Fig. S7.4 of Rödenbeck et al., 2013), but additionally takes into account that any data point in an already well-covered area has less individual effect. Though RoU is to some extent also influenced by our a-priori uncertainty settings (e.g., a smaller a-priori uncertainty would lower the achievable RoU, and the applied smoothness constraints carry information into unconstrained areas close to constrained ones), the patterns of Fig. 4 (bottom) should be broadly representative for SOCAT's information content on interannual anomalies, largely independently of the method used here.

3.3 Robustness

To exclude that the results are dominated by uncertain parameters or input data sets used in the calculation, Fig. 5 shows the envelope of a set of sensitivity results (Sect. 2.3.4), using the tropical Pacific as example region. Reflecting the fact that pCO_2 (middle panel) is the quantity directly constrained by the data, alterations in parameters only have a very small effect (sensitivity band much more narrow than the interannual variations). There are short periods of enhanced sensitivity in 2009 and before about 1992, when the tropical Pacific is less well constrained by the SOCAT data such that it stays closer to the prior and thus the effects of our sensitivity cases on the prior cannot be completely overwritten.

The sensitivity of the sea–air CO_2 fluxes (Fig. 5, top) is slightly enhanced compared to that of pCO_2, due to the direct effect of alterations in the gas exchange velocity. Still,

BGD
11, 3167–3207, 2014

despite some change in amplitude, the time course of the interannual flux variations is very robust.

Larger sensitivity is found in the ocean-internal DIC sources/sinks (Fig. 5, bottom). This is expected as any alteration in the parameterized relation between $f_{\text{int}}^{\text{DIC}}$ and $p\text{CO}_2$ enforces compensating changes in $f_{\text{int}}^{\text{DIC}}$. The biggest effect comes from the alterations in mixed-layer depth (MLD). Note however that our alterations of MLD by factors 2 and 0.5 are ad-hoc; this large range has been chosen to account for the missing interannual variations in MLD values used, but may overestimate the actual MLD errors.

In regions less well constrained than the tropical Pacific, estimates are less robust. Besides the above-mentioned effect that the alterations of the prior have more impact on the result, estimates in unconstrained regions critically depend on the choice of spatial correlation length: the longer the correlations, the farther variability from data-constrained locations is spread into unconstrained locations (see Fig. 5 of Rödenbeck et al., 2013). In particular, longer correlation carry the strong variability of the tropical Pacific farther into the poorly constrained areas south of it (Fig. 4, bottom), thus increasing the areal extent of this variability and leading to higher global IAV[5]. This leads to a sensitivity band for the global sea–air CO_2 fluxes (Fig. 3, bottom) that is somewhat wider than in the tropical Pacific. As the band is asymmetric, it suggests a somewhat lower amplitude of global IAV than in the standard case.

[5]The chosen length scale reflects both the size of coherent El Niño-related variations and the available information: even in the well-constrained equatorial Pacific, sufficient data coverage only exists at every 15° longitude (see Fig. 4, bottom) – if a shorter correlation scale is used, areas in between nearly revert back to the prior, leading to much smaller variations in the regional flux. Bridging these gaps through the correlations is justified as we expect longitudinally coherent variations here. In latitude direction, correlation lengths are chosen shorter reflecting the narrow size of El Niño-related features. Unfortunately, as the data coverage rapidly drops south of the equatorial region, both longer and shorter latitudinal correlation lengths lead to results equally compatible with the SOCAT data (they have similarly low residual bias, not shown), despite their differences in the IAV amplitude of the regional (or global) total.

BGD
11, 3167–3207, 2014

3.4 Interannual variability in the tropical Pacific

As the presented material establishes that the tropical Pacific is both a well-constrained and a globally important contributor to interannual sea–air CO_2 flux variability[6], we consider the contributions to the variability at different longitudes along the Equator (Fig. 6). During the 1993–2008 analysis period, fluxes at most longitudes are continuously constrained (left panel); the Western part even throughout the earlier years. The reduction of the flux during El Niño phases (middle, red colors) extends throughout considered part of the equatorial Pacific (200° W to 85° W), but with the tendency to be of smaller amplitude and to occur several months later in the East than in the West. This striking "propagation" can be confirmed statistically: the flux is significantly anti-correlated (Sect. 2.4) to the Multivariate El Niño Index (MEI, Wolter and Timlin, 1993, interannually filtered) at almost all longitudes (middle right panel, dark blue line), with a time lag increasing by more than half a year from West to East (top right panel; also see the example time series in the Fig. S4 for illustration).

Such a slow West-to-East "propagation" of sea–air CO_2 flux anomalies as constrained by SOCAT is not present in physical surface ocean variables: for example, SST is positively correlated to MEI, with almost no lag and propagating much faster (within about 1 month consistent with an equatorial Kelvin wave, not shown).[7] No slow "propagation" is thus found in the SST-dominated TE contribution either: consistent with Footnote 2 on page 6, the TE contribution is positively correlated to MEI as well (mid-

[6]Ocean regions other than the tropical Pacific either have much less IAV, or are not well constrained by the available pCO_2 observations (Fig. S1). Comparison with independent data at station HOT in the North Pacific broadly confirms the SOCAT-based anomalies, including the low IAV there (Sect. S3.3). Comparison at BATS is not successful in terms of interannual features, but still confirms the low amplitude in the North Atlantic as well (Sect. S3.3). Despite their lower IAV, various extratropical regions can be expected to play an important role in the long-term flux trend. A more detailed consideration warrants a separate study.

[7]In weak ENSO events, SST anomalies can even propagate westward, see Santoso et al. (2013).

BGD
11, 3167–3207, 2014

dle right panel, black line) and leads MEI by about 4 months at most longitudes (top right panel). However, also the OIS contribution (calculated by difference, light blue) shows a West-to-East "propagation" of only 1–2 months. This suggests that the slow "propagation" of the total anomalies is only an apparent one and does not arise from any actual propagation mechanism. Rather, as the amplitudes of the opposite TE and OIS contributions are markedly changing from West to East (bottom right panel), the temporal phase of their superposition is shifting (in the same way as sine and cosine Fourier terms of different relative weight add up to modes with different phase).

Can the remaining "propagation" in the OIS contribution arise from memory effects in the mixed-layer carbon budget? Anomalies in contribution OIS occur several months later than the causing anomalies in the ocean-interior DIC sources/sinks (not shown, but see the Fig. S4), due to the finite sea–air exchange rate enhanced by the buffer effect of carbonate chemistry. Anomalies in $f_{\mathrm{int}}^{\mathrm{DIC}}$ thus even lead MEI by 5–6 months, i.e., are associated with build-up or decline of the ENSO states. However, this delay between $f_{\mathrm{int}}^{\mathrm{DIC}}$ and $f_{\mathrm{ma}}^{\mathrm{CO_2}}$ is essentially the same throughout the equatorial Pacific, i.e., it does not contribute to the propagation.

3.5 Consistency to atmospheric oxygen observations

In order to relate the SOCAT-based IAV estimates to the information from atmospheric oxygen, the oceanic APO flux has been calculated from run *SFC* (Sect. 2.5). The information flow is illustrated in Fig. 7. Sea–air CO_2 flux ($f_{\mathrm{ma}}^{\mathrm{CO_2}}$, middle left) and ocean-interior carbon sources/sinks ($f_{\mathrm{int}}^{\mathrm{DIC}}$, bottom left) are constrained from SOCAT. Ocean-interior sources/sinks of oxygen ($f_{\mathrm{int}}^{\mathrm{O_2}}$, bottom right) are implied by those of carbon in the assumed Redfield proportion. Due to the short equilibration time of oxygen, anomalies in sea–air O_2 exchanges ($f_{\mathrm{ma}}^{\mathrm{O_2}}$, middle right) then follow $f_{\mathrm{int}}^{\mathrm{O_2}}$ closely. As interannual variations in sea–air CO_2 exchanges are much smaller than those in sea–air O_2 exchanges, the APO flux (Eq. 5, Fig. 7 top) dominantly reflects interannual variations in oxygen fluxes and thus in ocean-internal O_2 and DIC sources/sinks.

BGD
11, 3167–3207, 2014

The APO flux inferred from SOCAT is compared to that inferred from atmospheric oxygen data by a transport inversion (Rödenbeck et al., 2008, updated) (Fig. 7 top). Both of these independent estimates show enhanced APO outgassing during El Niño phases (grey stripes). While the SOCAT-based anomalies consistently lead ENSO events (due to the lead of $f_{\mathrm{int}}^{\mathrm{DIC}}$, compare Sect. 3.4), the APO-based anomalies coincide with the 1995 and 1997/98 ENSO events but also lead the 2009 event. Both estimates are of roughly similar amplitudes, though the relative heights of the anomalies in individual ENSO events are different.

Various conceivable error influences have the potential to distort the comparison: (1) Both the SOCAT and the APO constraints suffer from incomplete spatial coverage, where the regions of good coverage do not necessarily coincide. An APO inversion of "synthetic data" suggests that this may explain part of the differences in timing (Supplement, Sect. S4). (2) The information flow from the SOCAT data (Fig. 2) involves various uncertain model steps: even if run *SFC* would lead to a perfectly constrained $p_{\mathrm{m}}^{\mathrm{CO_2}}$ field, any errors in the parameterizations of carbonate chemistry (CC) and carbon budget (CB) would cause compensating spurious contributions to the internal DIC flux $f_{\mathrm{int}}^{\mathrm{DIC}}$ (compare Fig. 5) which then propagate to the calculated APO flux. A major simplification is the carbon-oxygen coupling (TT) assumed to be Redfieldian. Any errors in the oxygen budget (OB) and in the oxygen gas exchange (GE) additionally contribute, though their effect will be small due to the fast oxygen equilibration leading to $f_{\mathrm{ma}}^{\mathrm{O_2}} \approx f_{\mathrm{int}}^{\mathrm{O_2}}$ on interannual time scales. (3) The APO inversion involves various uncertainties both from necessary assumptions in the estimation and from observational error (Rödenbeck et al., 2008). Also, interannual variations in the sea–air N_2 (influencing the APO inversion because the atmospheric O_2 abundance is measured relative to the N_2 abundance) are neglected.

In the light of all these error influences, but also considering that the SOCAT and APO constraints are fully independent from each other in terms of both data and model, the partial agreement in the interannual APO flux variations is remarkable. Even though

BGD
11, 3167–3207, 2014

the comparison is not conclusive enough to provide a quantitative validation, we take it as a confirmation of plausibility of the mixed-layer scheme.

Conversely, the comparison also confirms that atmospheric oxygen observations contain information about ocean-internal carbon sources/sinks and thus sea–air CO_2 exchange. To use this information as an additional constraint, we need to tackle the error influences listed above, in particular (1) increase the information from atmospheric oxygen by adding existing or new observation sites, (2) use a more realistic representation of carbon-oxygen coupling (TT) which may involve further data sources. In any case, a crucial role is played by the availability of atmospheric oxygen records that cover the entire time period under consideration without interruption.

3.6 Comparison to simulations by an ocean process model – IAV and trend

The data-based estimates presented here can be used to challenge the results of process simulations for well-constrained features, but conversely, comprehensive process models can be used to challenge our results where constraints are weak such that we rely on our simple parameterizations. Therefore, sea–air CO_2 fluxes have been calculated from pCO_2 simulations by an ocean biogeochemical process model run (NEMOv2.3 with PlankTOM5, Buitenhuis et al., 2010) (but using the same gas exchange parametrizations as in our diagnostic scheme). As in the SOCAT-based run *SFC*, the total ocean flux variability (Fig. 8) is strongly tied to ENSO. Though the process model gives a smaller amplitude than *SFC* (about half), this model is the one with the largest interannual variability among the suite of process models considered in Wanninkhof et al. (2013) (their Fig. 6), and agrees by far the best with our SOCAT-based estimate.

In both the model simulation and our data-based run *SFC*, total ocean flux variability is dominated by the tropical Pacific, where both estimates are in closest agreement (Supplement, Fig. S2). The estimates further agree that all other regions have smaller IAV, though there is hardly any correspondence in the detailed features. The regional comparison reveals that the differences in global amplitude are to large extent related

BGD
11, 3167–3207, 2014

to areas south of the tropical Pacific, reinforcing the possibility that our amplitude is overestimated due to the tropical variability being spread over too great an area (end of Sect. 3.3).

Rising atmospheric CO_2 content leads to rising CO_2-undersaturation of the global ocean and thus an increasing oceanic sink. The magnitude of this trend, however, cannot be predicted from simple considerations as it critically depends on the rate by which the sequestered carbon is passed on from the surface ocean into the interior. Therefore process model simulations are needed. From a suite of models, Le Quéré et al. (2013) (Global Carbon Project, GCP) give a sink time series increasing by $-0.032\,(\mathrm{Pg\,C\,yr^{-1}})\,\mathrm{yr^{-1}}$ over 1960–2012 (linear fit, converted to atmospheric sign convention). While the period of good data coverage is too short to compare this long-term trend, both our data-based estimates, NEMO-PlankTOM5, and the GCP model mean agree that the 1990–1999 period saw a negligible or even reversed trend, followed by the 2000–2009 period with a trend almost 50 % stronger than long-term (trend lines in Fig. 8, also see Fig. 5c of Le Quéré et al., 2013). Unfortunately, a more quantitative analysis of these short-term trends is difficult due to the large interannual variability and region-to-region differences (e.g., Fay and McKinley, 2013).

3.7 Combination with an atmospheric CO_2 inversion – implication for land flux estimates

Interannual variations of regional sea–air CO_2 fluxes can also be estimated from atmospheric CO_2 mixing ratio measurements by atmospheric transport inversion (Newsam and Enting, 1988; Rayner et al., 1999). However, the atmospheric signal is dominated by the much larger variability of land–atmosphere CO_2 fluxes. Though the total (land+ocean) flux within latitude bands is relatively well-constrained from atmospheric CO_2 data (due to atmospheric tracer mass conservation and the predominantly longitudinal tracer transport in the atmosphere), errors in the attribution to land or ocean, even if small compared to the land fluxes, can have a large relative impact on the smaller ocean fluxes. Indeed, we do not find much similarity between the SOCAT-based flux

BGD
11, 3167–3207, 2014

estimates and an atmospheric inversion (Fig. 9, top): the ocean total from the atmospheric inversion is almost anti-correlated to run *SFC*, but rather more in phase with land biosphere variability (see Fig. 9, bottom), suggesting that these variations are spuriously spilling over from there. This is in line with a relatively large spread in the ocean fluxes from different atmospheric inversions (see the RECCAP ensemble, Peylin et al., 2013), confirming a limited constraint of the atmospheric data on land/ocean flux partitioning. Similar discrepancies between SOCAT-based and atmospheric inversion estimates are also found in regional fluxes (Supplement, Fig. S3), though at least the relative amplitudes of flux IAV between the regions broadly agree. Surprisingly similar variations are found in the tropical Indian.

As the SOCAT-based estimates show more plausible ocean flux IAV than the atmospheric inversion at least in the region contributing the largest variability (Equatorial Pacific), it would be beneficial to add pCO_2 as further constraint to the atmospheric inversion: due to the atmospheric mass conservation, land flux estimates profit from any improvement in the poorly constrained ocean fluxes. Even though interannual variations outside the Equatorial Pacific are not well constrained from the pCO_2 data in many places and thus stay close to the prior of the diagnostic scheme (Sect. 3.2), they still contain the temperature-related part as represented in the parametrizations. In practical terms, even in areas where this is a bad approximation, using the SOCAT-based estimates will not worsen the land fluxes from the atmospheric inversion much (compared to an inversion with a freely adjustable ocean flux) due to their small amplitude. Only in the Southern Ocean where influence from adjacent land regions is smallest, the constraint from atmospheric CO_2 data may be powerful, and able to compensate the weakness of the pCO_2 constraint there.

The inclusion of the pCO_2 constraint into the atmospheric inversion can be implemented by adding together the cost function contributions of pCO_2 data (from *SFC*) and of atmospheric CO_2 (see the companion paper Rödenbeck et al., 2013, Appendix A2.3). However, as the ocean fluxes are much more strongly constrained by the pCO_2 data rather than the atmospheric data, such a joint inversion gives ocean

BGD
11, 3167–3207, 2014

fluxes almost identical to run *SFC* (test run not shown)[8]. Given this, we may simply use the results of run *SFC* as a fixed ocean prior in a subsequent "classical" atmospheric inversion in which only the land fluxes are adjusted, which is much more practical[9]. Figure 9 (bottom) compares total land CO_2 fluxes from atmospheric inversions with adjustable or fixed ocean fluxes. Using the SOCAT-based run *SFC* as prior slightly increases the land flux IAV. This is largely due to differences in South America (Fig. S3) where the density of atmospheric measurement sites is low, such that the distinction of land and ocean fluxes is not well constrained in the "classical" atmospheric inversion. Differences also occur in the Asian regions. However, the impact is still roughly within the range of many other uncertainties in global atmospheric CO_2 inversions (e.g., see the spread of results by various inversion studies participating in the RECCAP ensemble, Peylin et al., 2013).

Future developments of carbon cycle quantification should use the good constraint of pCO_2 data on the tropical Pacific and much of the Northern extratropics, but also the constraint of atmospheric CO_2 data on the Southern Ocean. Further, a joint CO_2 and APO inversion, linking sea–air CO_2 and O_2 fluxes through the diagnostic mixed-layer scheme, would exploit the potential of atmospheric oxygen observations to constrain the ocean-internal processes driving the sea–air CO_2 flux variability as demonstrated in Sect. 3.5. The APO constraint applies on the same large spatial scales that drive the air–sea CO_2 flux variability, and thus would be a valuable complement to the pCO_2 and atmospheric CO_2 data in the previously underconstrained areas.

[8] A similar situation was found in the joint inversion by Jacobson et al. (2007) considering long-term fluxes.

[9] The sequential estimation is much more efficient because the pCO_2 constraint needs many more iterations in the cost function minimization (about 200) than the atmospheric inversion (about 70). A combined inversion would require the expensive transport model runs for all these additional iterations.

BGD
11, 3167–3207, 2014

4 Conclusions

Based on the SOCAT v2 data set of pCO_2 observations, we estimated interannual variations of the sea–air CO_2 exchange, using a data-driven diagnostic scheme of mixed-layer carbon biogeochemistry as a space-time interpolator. The scheme links sea–air CO_2 exchange to ocean-internal DIC sources and sinks, thereby also allowing to relate carbon anomalies to signals in oxygen (or nutrient) observations.

- SOCAT pCO_2 data constrain interannual variations in the sea–air CO_2 flux in parts of the ocean, notably in the tropical Pacific where the largest interannual variations are found.
- The tropical Pacific shows a reduced CO_2 outgassing during El Niño phases. In the East, this anomaly occurs more than 6 months later than in the West, likely due to different relative contributions of temperature-related and biologically/physically caused responses.
- The SOCAT-based estimates of the interannual variations in tropical sea–air CO_2 flux and ocean-internal DIC sources/sinks are broadly consistent with the independent constraint from atmospheric oxygen measurements.
- In qualitative agreement with ocean process model simulations, the ocean sink in the SOCAT-based estimates increases less than expected from atmospheric CO_2 rise during 1990–1999 and more than expected during 2000–2009.
- Surface-ocean pCO_2 data constrain interannual variations in sea–air CO_2 fluxes better than atmospheric CO_2 data, at least for the dominating variations in the tropical Pacific. The pCO_2-based estimates can be used as ocean prior in atmospheric CO_2 inversions to improve their land flux estimates.

The presented gridded sea–air CO_2 flux estimates can be downloaded in digital form from the Jena inversion web-site, http://www.bgc-jena.mpg.de/~christian.roedenbeck/download-CO2-ocean/ (version "oc_v1.2"). Regular updates are planned.

BGD
11, 3167–3207, 2014

Supplementary material related to this article is available online at http://www.biogeosciences-discuss.net/11/3167/2014/bgd-11-3167-2014-supplement.pdf.

Acknowledgements. We would like to thank all contributors to the SOCAT data base, the operators of the HOT and BATS time series stations, as well as all providers of atmospheric CO_2 data, which are the basis of this work. We gratefully acknowledge helpful discussions with Nick Bates, Andrew Dickson, Niki Gruber, Roberta Hamme, Steve Jones, Bob Key, Armin Köhl, Corinne Le Quéré (who also provided the process model results), Sara Mikaloff Fletcher, Bill Munger, Andreas Oschlies, Gilles Reverdin, Keith Rodgers, Taro Takahashi, Yasunori Tohjima, and Lisan Yu. This study was also supported through EU FP7 project CARBOCHANGE (264879) and is a contribution to the international IMBER/SOLAS projects. D.C.E.B. received support from the UK Ocean Acidification Research Programme (NE/H017046/1). N.M. also thanks CNRS/INSU for supporting the SURATLANT project. A.O. appreciates support from the Centre for Climate Dynamics at the Bjerknes Centre for Climate Research.

The service charges for this open access publication have been covered by the Max Planck Society.

References

Anderson, L.: On the hydrogen and oxygen content of marine phytoplankton, Deep-Sea Res. Pt. I, 42, 1675–1680, 1995. 3177

Arthun, M., Bellerby, R. G. J., Omar, A. M., and Schrum, C.: Spatiotemporal variability of air–sea CO_2 fluxes in the Barents Sea, as determined from empirical relationships and modeled hydrography, J. Marine Syst., 98-99, 40–50, doi:10.1016/j.jmarsys.2012.03.005, 2012.

Bakker, D. C. E., Pfeil, B., Smith, K., Hankin, S., Olsen, A., Alin, S. R., Cosca, C., Harasawa, S., Kozyr, A., Nojiri, Y., O'Brien, K. M., Schuster, U., Telszewski, M., Tilbrook, B., Wada, C., Akl, J., Barbero, L., Bates, N., Boutin, J., Cai, W.-J., Castle, R. D., Chavez, F. P., Chen, L., Chierici, M., Currie, K., de Baar, H. J. W., Evans, W., Feely, R. A., Fransson, A.,

Gao, Z., Hales, B., Hardman-Mountford, N., Hoppema, M., Huang, W.-J., Hunt, C. W., Huss, B., Ichikawa, T., Johannessen, T., Jones, E. M., Jones, S. D., Jutterström, S., Kitidis, V., Körtzinger, A., Landschtzer, P., Lauvset, S. K., Lefèvre, N., Manke, A. B., Mathis, J. T., Merlivat, L., Metzl, N., Murata, A., Newberger, T., Ono, T., Park, G.-H., Paterson, K., Pierrot, D., Ríos, A. F., Sabine, C. L., Saito, S., Salisbury, J., Sarma, V. V. S. S., Schlitzer, R., Sieger, R., Skjelvan, I., Steinhoff, T., Sullivan, K., Sun, H., Sutton, A. J., Suzuki, T., Sweeney, C., Takahashi, T., Tjiputra, J., Tsurushima, N., van Heuven, S. M. A. C., Vandemark, D., Vlahos, P., Wallace, D. W. R., Wanninkhof, R., and Watson, A. J.: An update to the Surface Ocean CO_2 Atlas (SOCAT version 2), Earth Syst. Sci. Data Discuss., 6, 465–512, doi:10.5194/essdd-6-465-2013, 2013. 3171

Bates, N. R., Best, M. H. P., Neely, K., Garley, R., Dickson, A. G., and Johnson, R. J.: Detecting anthropogenic carbon dioxide uptake and ocean acidification in the North Atlantic Ocean, Biogeosciences, 9, 2509–2522, doi:10.5194/bg-9-2509-2012, 2012.

Buitenhuis, E., Rivkin, R., Sailley, S., and Le Quéré, C.: Biogeochemical fluxes through microzooplankton, Global Biogeochem. Cy., 24, GB4015, doi:10.1029/2009GB003601, 2010. 3186, 3206

Chevallier, F., Bréon, F.-M., and Rayner, P. J.: Contribution of the Orbiting Carbon Observatory to the estimation of CO_2 sources and sinks: theoretical study in a variational data assimilation framework, J. Geophys. Res., 112, D09307, doi:10.1029/2006JD007375, 2007. 3174

Conkright, M., Locarnini, R. A., Garcia, H., O'Brien, T., Boyer, T., Stephens, C., and Antonov, J.: World Ocean Atlas 2001: Objective Analyses, Data Statistics, and Figures, CD-ROM Documentation, National Oceanographic Data Center, Silver Spring, MD, 17 pp., 2002. 3198

Corbière, A., Metzl, N., Reverdin, G., Brunet, C., and Takahashi, T.: Interannual and decadal variability of the oceanic carbon sink in the North Atlantic subpolar gyre, Tellus B, 59, 168–178, 2007.

de Boyer Montégut, C., Madec, G., Fischer, A. S., Lazar, A., and Iudicone, D.: Mixed layer depth over the global ocean: an examination of profile data and a profile-based climatology, J. Geophys. Res., 109, C12003, doi:10.1029/2004JC002378, 2004. 3198

Dore, J., Lukas, R., Sadler, D., Church, M., and Karl, D.: Physical and biogeochemical modulation of ocean acidification in the central North Pacific, P. Natl. Acad. Sci. USA, 106, 12235–12240, 2009.

BGD
11, 3167–3207, 2014

Egleston, E. S., Sabine, C. L., and Morel, F. M. M.: Revelle revisited: buffer factors that quantify the response of ocean chemistry to changes in DIC and alkalinity, Global Biogeochem. Cy., 24, GB1002, doi:10.1029/2008GB003407, 2010. 3198

Fay, A. R. and McKinley, G. A.: Global trends in surface ocean pCO_2 from in situ data, Global Biogeochem. Cy., 27, 541–557, doi:10.1002/gbc.20051, 2013. 3187

Feely, R. A., Wanninkhof, R., Takahashi, T., and Tans, P.: Influence of El Niño on the equatorial Pacific contribution to atmospheric CO_2 accumulation, Nature, 398, 597–601, 1999. 3180

Feely, R., Boutin, J., Cosca, C., Dandonneau, Y., Etcheto, J., Inoue, H., Ishii, M., Quéré, C. L., Mackey, D., McPhaden, M., Metzl, N., Poisson, A., and Wanninkhov, R.: Seasonal and interannual variability of CO_2 in the Equatorial Pacific, Deep-Sea Res. Pt. II, 49, 2443–2469, doi:10.1016/S0967-0645(02)00044-9, 2002. 3180

Garcia, H. E., Locarnini, R. A., Boyer, T. P., and Antonov, J. I.: World Ocean Atlas 2005, Volume 3: Dissolved oxygen, apparent oxygen utilization, and oxygen saturation, in: NOAA Atlas NESDIS 63, edited by: Levitus, S., US Government Printing Office, Washington DC, 2006. 3178

Inoue, H., Ishii, M., Matsueda, H., Saito, S., Aoyama, M., Tokieda, T., Midorikawa, T., Nemoto, K., Kawano, T., Asanuma, I., Ando, K., Yano, T., and Murata, A.: Distributions and variations in the partial pressure of CO_2 in surface waters (pCO_2^w) of the central and western equatorial Pacific during the 1997/1998 El Niño event, Mar. Chem., 76, 59–75, 2001. 3180

Jacobson, A. R., Mikaloff Fletcher, S. E., Gruber, N., Sarmiento, J. L., and Gloor, M.: A joint atmosphere–ocean inversion for surface fluxes of carbon dioxide: 1. Methods and global-scale fluxes, Global Biogeochem. Cy., 21, GB1019, doi:10.1029/2005GB002556, 2007. 3189

Kalnay, E., Kanamitsu, M., Kistler, R., Collins, W., Deaven, D., Gandin, L., Iredell, M., Saha, S., White, G., Woollen, J., Zhu, Y., Chelliah, M., Ebisuzaki, W., Higgins, W., Janowiak, J., Mo, K. C., Ropelewski, C., Wang, J., Leetmaa, A., Reynolds, R., Jenne, R., and Joseph, D.: The NCEP/NCAR 40-year reanalysis project, B. Am. Meteorol. Soc., 77, 437–471, 1996. 3198

Keeling, R. F.: Development of an interferometric oxygen analyzer for precise measurement of the atmospheric O_2 mole fraction, Ph.D. thesis, Harvard Univ., Cambridge, USA, 1988. 3179

Keeling, R. F. and Shertz, S. R.: Seasonal and interannual variations in atmospheric oxygen and implications for the global carbon cycle, Nature, 358, 723–727, 1992. 3170

Key, R. M., Kozyr, A., Sabine, C. L., Lee, K., Wanninkhof, R., Bullister, J. L., Feely, R. A., Millero, F. J., Mordy, C., and Peng, T.-H.: A global ocean carbon climatology: results

BGD
11, 3167–3207, 2014

from Global Data Analysis Project (GLODAP), Global Biogeochem. Cy., 18, GB4031, doi:10.1029/2004GB002247, 2004. 3198

Le Quéré, C., Peters, G. P., Andres, R. J., Andrew, R. M., Boden, T., Ciais, P., Friedlingstein, P., Houghton, R. A., Marland, G., Moriarty, R., Sitch, S., Tans, P., Arneth, A., Arvanitis, A., Bakker, D. C. E., Bopp, L., Canadell, J. G., Chini, L. P., Doney, S. C., Harper, A., Harris, I., House, J. I., Jain, A. K., Jones, S. D., Kato, E., Keeling, R. F., Klein Goldewijk, K., Körtzinger, A., Koven, C., Lefèvre, N., Omar, A., Ono, T., Park, G.-H., Pfeil, B., Poulter, B., Raupach, M. R., Regnier, P., Rödenbeck, C., Saito, S., Schwinger, J., Segschneider, J., Stocker, B. D., Tilbrook, B., van Heuven, S., Viovy, N., Wanninkhof, R., Wiltshire, A., Zaehle, S., and Yue, C.: Global carbon budget 2013, Earth Syst. Sci. Data Discuss., 6, 689–760, doi:10.5194/essdd-6-689-2013, 2013. 3187

Lee, K., Tong, L. T., Millero, F. J., Sabine, C. L., Dickson, A. G., Goyet, C., Park, G.-H., Wanninkhof, R., Feely, R. A., and Key, R. M.: Global relationships of total alkalinity with salinity and temperature in surface waters of the world's oceans, Geophys. Res. Lett., 33, L19605, doi:10.1029/2006GL027207, 2006. 3198

Metzl, N., Corbière, A., Reverdin, G., Lenton, A., Takahashi, T., Olsen, A., Johannessen, T., Pierrot, D., Wanninkhof, R., Ólafsdóttir, S. R., Olafsson, J., and Ramonet, M.: Recent acceleration of the sea surface fCO_2 growth rate in the North Atlantic subpolar gyre (1993–2008) revealed by winter observations, Global Biogeochem. Cy., 24, GB4004, doi:10.1029/2009GB003658, 2010.

Monahan, E. C. and Torgersen, T.: Enhancement of air–sea gas exchange by oceanic whitecapping, in: Air–Water Mass Transfer: Selected Papers from the Second International Symposium on Gas Transfer at Water Surfaces, edited by: Wilhelms, S. C. and Gulliver, J. S., American Society of Civil Engineering, New York, 608–617, 1990. 3178

Naegler, T.: Reconciliation of excess ^{14}C-constrained global CO_2 piston velocity estimates, Tellus B, 61, 372–384, 2009. 3176

Newsam, G. N. and Enting, I. G.: Inverse problems in atmospheric constituent studies: I. Determination of surface sources under a diffusive transport approximation, Inverse Probl., 4, 1037–1054, 1988. 3187

Peylin, P., Law, R. M., Gurney, K. R., Chevallier, F., Jacobson, A. R., Maki, T., Niwa, Y., Patra, P. K., Peters, W., Rayner, P. J., Rödenbeck, C., van der Laan-Luijkx, I. T., and Zhang, X.: Global atmospheric carbon budget: results from an ensemble of atmospheric CO_2 inversions, Biogeosciences, 10, 6699–6720, doi:10.5194/bg-10-6699-2013, 2013. 3188, 3189

BGD
11, 3167–3207, 2014

Pfeil, B., Olsen, A., Bakker, D. C. E., Hankin, S., Koyuk, H., Kozyr, A., Malczyk, J., Manke, A., Metzl, N., Sabine, C. L., Akl, J., Alin, S. R., Bates, N., Bellerby, R. G. J., Borges, A., Boutin, J., Brown, P. J., Cai, W.-J., Chavez, F. P., Chen, A., Cosca, C., Fassbender, A. J., Feely, R. A., González-Dávila, M., Goyet, C., Hales, B., Hardman-Mountford, N., Heinze, C., Hood, M., Hoppema, M., Hunt, C. W., Hydes, D., Ishii, M., Johannessen, T., Jones, S. D., Key, R. M., Körtzinger, A., Landschützer, P., Lauvset, S. K., Lefèvre, N., Lenton, A., Lourantou, A., Merlivat, L., Midorikawa, T., Mintrop, L., Miyazaki, C., Murata, A., Nakadate, A., Nakano, Y., Nakaoka, S., Nojiri, Y., Omar, A. M., Padin, X. A., Park, G.-H., Paterson, K., Perez, F. F., Pierrot, D., Poisson, A., Ríos, A. F., Santana-Casiano, J. M., Salisbury, J., Sarma, V. V. S. S., Schlitzer, R., Schneider, B., Schuster, U., Sieger, R., Skjelvan, I., Steinhoff, T., Suzuki, T., Takahashi, T., Tedesco, K., Telszewski, M., Thomas, H., Tilbrook, B., Tjiputra, J., Vandemark, D., Veness, T., Wanninkhof, R., Watson, A. J., Weiss, R., Wong, C. S., and Yoshikawa-Inoue, H.: A uniform, quality controlled Surface Ocean CO_2 Atlas (SOCAT), Earth Syst. Sci. Data, 5, 125–143, doi:10.5194/essd-5-125-2013, 2013. 3169, 3171

Rayner, P., Enting, I., Francey, R., and Langenfelds, R.: Reconstructing the recent carbon cycle from atmospheric CO_2, $\delta^{13}CO_2$ and O_2/N_2 observations, Tellus B, 51, 213–232, 1999. 3187

Rödenbeck, C.: Estimating CO_2 sources and sinks from atmospheric mixing ratio measurements using a global inversion of atmospheric transport, Tech. Rep. 6, Max Planck Institute for Biogeochemistry, Jena, Germany, 2005. 3171, 3172

Rödenbeck, C., Le Quéré, C., Heimann, M., and Keeling, R.: Interannual variability in oceanic biogeochemical processes inferred by inversion of atmospheric O_2/N_2 and CO_2 data, Tellus B, 60, 685–705, 2008. 3170, 3177, 3178, 3179, 3185, 3200, 3205

Rödenbeck, C., Keeling, R. F., Bakker, D. C. E., Metzl, N., Olsen, A., Sabine, C., and Heimann, M.: Global surface-ocean pCO_2 and sea–air CO_2 flux variability from an observation-driven ocean mixed-layer scheme, Ocean Sci., 9, 193–216, doi:10.5194/os-9-193-2013, 2013. 3169, 3171, 3173, 3175, 3177, 3178, 3181, 3182, 3188, 3198, 3199

Sabine, C., Maenner, S., and Sutton, A.: High-resolution ocean and atmosphere pCO_2 time-series measurements from mooring TAO140W, http://cdiac.esd.ornl.gov/ftp/oceans/Moorings/TAO140W/, Carbon Dioxide Information Analysis Center, Oak Ridge National Laboratory, US Department of Energy, Oak Ridge, Tennessee, doi:10.3334/CDIAC/otg.TSM_TAO140W, 2010.

BGD
11, 3167–3207, 2014

Santoso, A., McGregor, S., Jin, F.-F., Cai, W., England, M. H., An, S.-I., McPhaden, M. J., and Guilyardi, E.: Late-twentieth-century emergence of the El Niño propagation asymmetry and future projections, Nature, 504, 126–130, 2013. 3183

Sarmiento, J. L. and Gruber, N.: Ocean Biogeochemical Dynamics, Princeton Univ. Press, 2006. 3171

Sarmiento, J. L., Gloor, M., Gruber, N., Beaulieu, C., Jacobson, A. R., Mikaloff Fletcher, S. E., Pacala, S., and Rodgers, K.: Trends and regional distributions of land and ocean carbon sinks, Biogeosciences, 7, 2351–2367, doi:10.5194/bg-7-2351-2010, 2010. 3169

Stanley, R. H. R., Jenkins, W. J., Lott III, D. E., and Doney, S. C.: Noble gas constraints on air–sea gas exchange and bubble fluxes, J. Geophys. Res., 114, C11020, doi:10.1029/2009JC005396, 2009. 3178

Stephens, B. B., Keeling, R. F., Heimann, M., Six, K. D., Murnane, R., and Caldeira, K.: Testing global ocean carbon cycle models using measurements of atmospheric O_2 and CO_2 concentration, Global Biogeochem. Cy., 12, 213–230, 1998. 3179

Takahashi, T., Sutherland, S. C., Wanninkhof, R., Sweeney, C., Feely, R. A., Chipman, D. W., Hales, B., Friederich, G., Chavez, F., Sabine, C., Watson, A., Bakker, D. C. E., Schuster, U., Metzl, N., Yoshikawa-Inoue, H., Ishii, M., Midorikawa, T., Nojiri, Y., Kortzinger, A., Steinhoff, T., Hoppema, M., Olafsson, J., Arnarson, T. S., Tillbrook, B., Johannessen, T., and Olsen, A., Bellerby, R., Wong, C. S., Delille, B., Bates, N. R., and de Baar, H. J. W.: Climatological mean and decadal change in surface ocean pCO_2 and net sea–air CO_2 flux over the global oceans, Deep-Sea Res. II, 56, 554–577, 2009. 3170, 3172

Tarantola, A.: Inverse Problem Theory, Methods for Data Fitting and Model Parameter Estimation, Elsevier, New York, 1987.

Wanninkhof, R.: Relationship between wind speed and gas exchange over the ocean, J. Geophys. Res.-Oceans, 97, 7373–7382, 1992. 3171

Wanninkhof, R., Park, G. -H., Takahashi, T., Sweeney, C., Feely, R., Nojiri, Y., Gruber, N., Doney, S. C., McKinley, G. A., Lenton, A., Le Quéré, C., Heinze, C., Schwinger, J., Graven, H., and Khatiwala, S.: Global ocean carbon uptake: magnitude, variability and trends, Biogeosciences, 10, 1983–2000, doi:10.5194/bg-10-1983-2013, 2013. 3186

Watson, A. J., Schuster, U., Bakker, D. C. E., Bates, N. R., Corbiére, A., González-Dávila, M., Friedrich, T., Hauck, J., Heinze, C., Johannessen, T., Körtzinger, A., Metzl, N., Olafsson, J., Olsen, A., Oschlies, A., Padin, X. A., Pfeil, B., Santana-Casiano, J. M., Steinhoff, T., Telszewski, M., Rios, A. F., Wallace, D. W. R., and Wanninkhof, R.: Tracking the variable North

BGD
11, 3167–3207, 2014

Atlantic sink for atmospheric CO_2, Science, 326, 1391–1393, doi:10.1126/science.1177394, 2009. 3180

Weiss, R.: Carbon dioxide in water and seawater: the solubility of a non-ideal gas, Mar. Chem., 2, 203–205, 1974. 3171

Wolter, K. and Timlin, M.: Monitoring ENSO in COADS with a seasonally adjusted principal component index, in: Proceedings of the 17th Climate Diagnostics Workshop, Norman, OK, NOAA/NMC/CAC, NSSL, Oklahoma Clim. Survey, CIMMS and the School of Meteor., Univ. of Oklahoma, 52–57, 1993. 3176, 3183, 3204

Yu, L. and Weller, R. A.: Objectively Analyzed air–sea heat Fluxes (OAFlux) for the global oceans, B. Am. Meteorol. Soc., 88, 527–539, 2007. 3198

BGD
11, 3167–3207, 2014

Table 1. Data sets used as driver fields in the parameterizations of sea–air gas exchange, solubility, and carbonate chemistry (see Rödenbeck et al., 2013).

Quantity	Data set	Reference
Wind speed	NCEP reanalysis	Kalnay et al. (1996)
Sea Surface Temperature	OAFlux	Yu and Weller (2007)
Ice-free fraction	OAFlux	Yu and Weller (2007)
Mixed-layer depth (climatology)	LOCEAN	de Boyer Montégut et al. (2004)
Salinity (climatology)	WOA 2001	Conkright et al. (2002)
Alkalinity (climatology)		Lee et al. (2006)
Buffer factor		Egleston et al. (2010)
Reference DIC concentration	GLODAP	Key et al. (2004)

Glossary: GLODAP = Global Ocean Data Analysis Project; LOCEAN = Laboratoire d'océanographie et du climat: expérimentations et approches numériques; NCEP = National Centers for Environmental Prediction; OAFlux = Objectively Analysed air–sea Fluxes; WOA = World Ocean Atlas.

BGD
11, 3167–3207, 2014

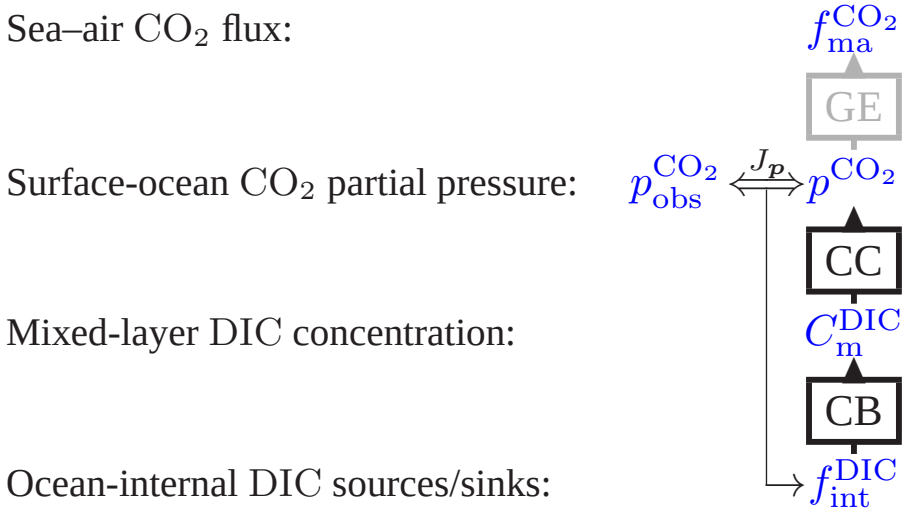

Fig. 1. Illustration of the inverse procedure in our main case (run *SFC*): boxes denote the process representations causally linking quantities from bottom to top: mixed-layer carbon budget (CB), carbonate chemistry (CC), solubility and sea–air gas exchange (GE). The double arrow symbolizes the matching between observed and modelled CO_2 partial pressure, as gauged by the cost function J_p. The thin arrow indicates the adjustments of the unknown ocean-internal carbon sources/sinks done to minimize the model–data mismatch (see Rödenbeck et al., 2013, for full details).

BGD
11, 3167–3207, 2014

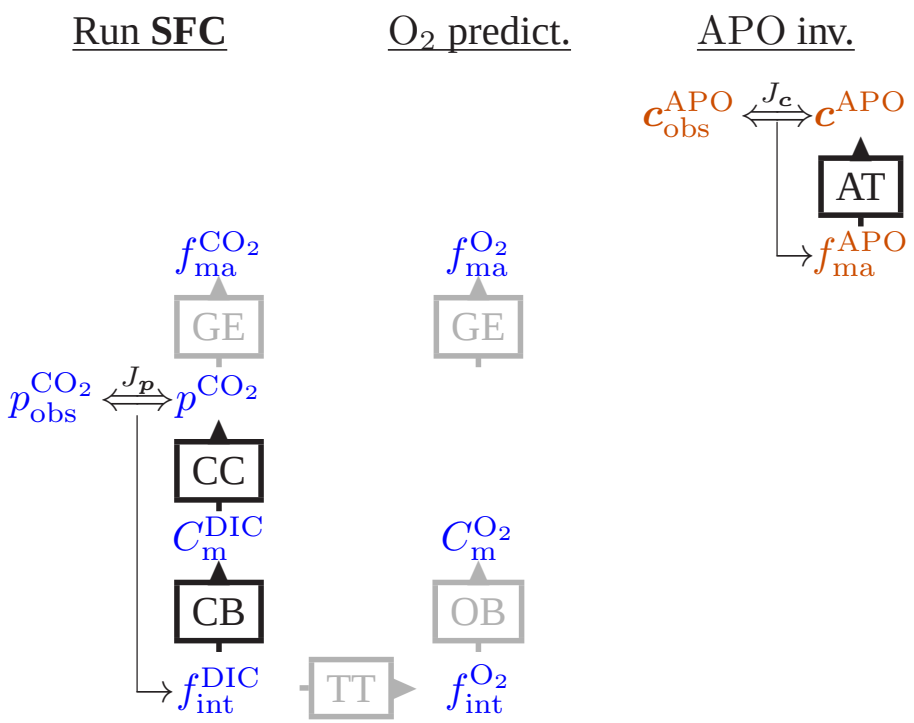

Fig. 2. Information flow between carbon and oxygen variables. Left: inverse procedure of run *SFC* as in Fig. 1, estimating ocean-internal DIC sources/sinks from pCO_{2m} data. Middle: prediction of the oxygen sea–air flux: ocean-internal oxygen sources/sinks are calculated from DIC sources/sinks via tracer-tracer coupling (TT) assumed to follow Redfield stoichiometries. Dissolved oxygen concentration ($C_m^{O_2}$) and sea–air oxygen flux ($f_{ma}^{O_2}$) are then obtained from parameterizations of an mixed-layer oxygen budget (OB), as well as oxygen solubility and sea–air gas exchange (GE), analogous to those for carbon. Right: APO inversion of Rödenbeck et al. (2008): sea–air APO fluxes are estimated from APO observations (combined atmospheric oxygen and CO_2 data) by inversion of atmospheric transport (AT).

BGD
11, 3167–3207, 2014

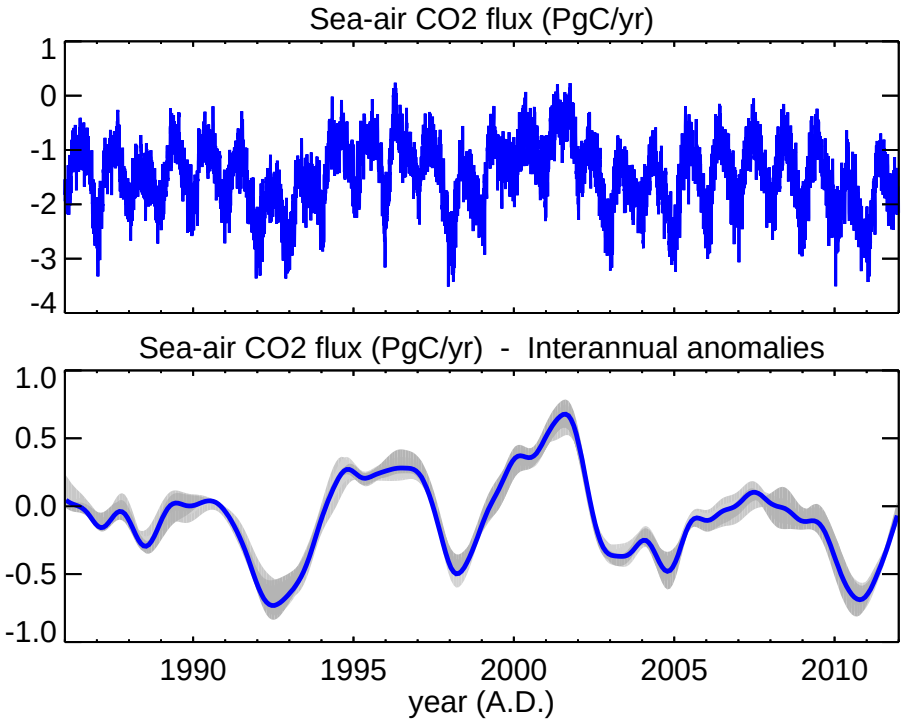

Fig. 3. Top: globally integrated sea–air CO_2 exchange estimated from SOCAT data (run *SFC*, blue). Negative values indicate an ocean CO_2 sink. Bottom: interannual anomalies of the globally integrated sea–air CO_2 exchange. The time series have been deseasonalized and filtered for interannual variations, and the 1993–2008 mean flux has been subtracted (positive values indicate an increased ocean CO_2 source or a decreased sink). The light-grey band around the standard case comprises a set of sensitivity cases (Sect. 2.3.4). The time period shown excludes the first year for spin-up, and the years after the end of SOCAT v2 (end of 2011).

BGD
11, 3167–3207, 2014

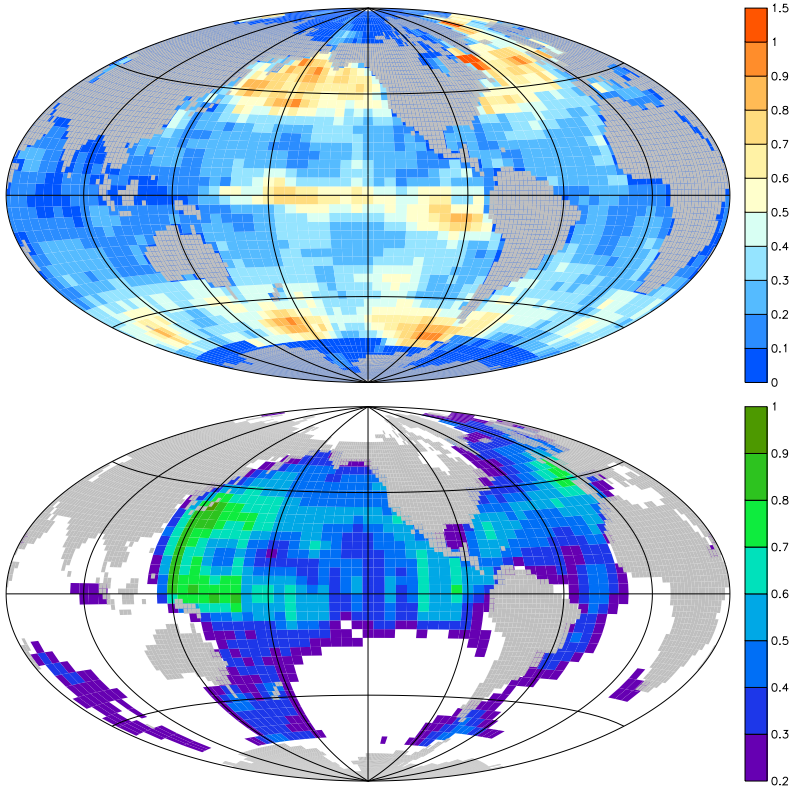

Fig. 4. Top: amplitude of IAV of the sea–air CO_2 flux estimated from SOCAT data (run *SFC*), calculated as temporal standard deviation (1993–2008) of the interannually filtered flux ($\mu mol\,m^{-2}\,yr^{-1}$). Bottom: capacity of the diagnostic scheme to retrieve interannual variations in the sea–air CO_2 flux from SOCAT v2.0 data (Reduction of Uncertainty, average performance 1993–2008). Pixels with RoU < 0.2 have been left uncolored.

BGD
11, 3167–3207, 2014

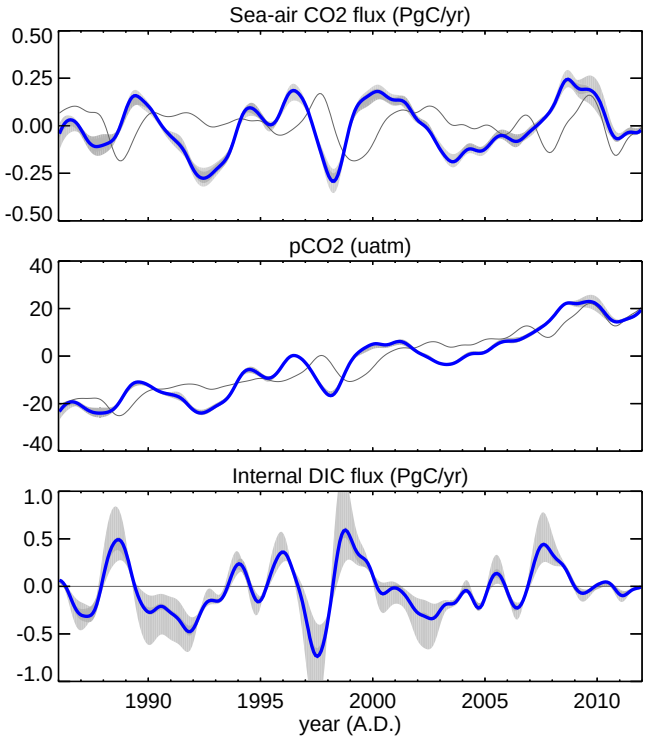

Fig. 5. Interannual carbon anomalies in the tropical Pacific (15° S–15° N) from run *SFC* (blue, filter and grey uncertainty band as in Fig. 3): top: sea–air CO_2 flux anomalies ($f_{ma}^{CO_2}$), middle: surface CO_2 partial pressure anomalies (pCO_2), bottom: anomalies in the ocean-internal DIC sources and sinks (f_{int}^{DIC}, note vertical scale different from $f_{ma}^{CO_2}$). The dark grey lines give the a-priori state of the diagnostic scheme only responding to changes in the driving variables (predominantly temperature).

BGD
11, 3167–3207, 2014

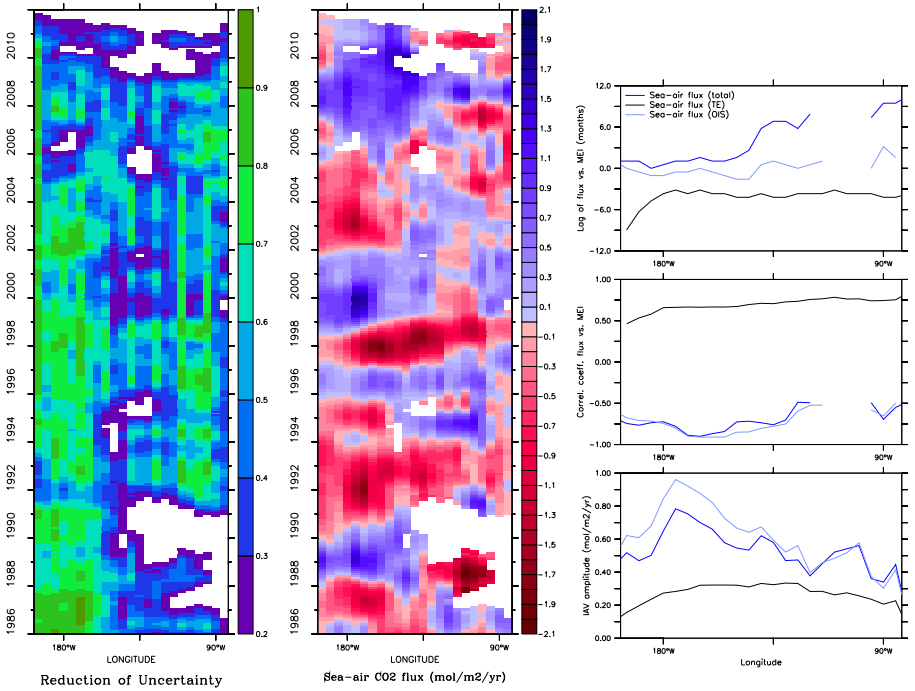

Fig. 6. Sea–air CO_2 flux variability along the Equator in the Pacific (4° S–4° N average). Left: strength of the data constraint (RoU). Middle: interannual anomalies of sea–air CO_2 flux shown as Hovmöller plot (color-coded over longitude (horizontal axis) and time (vertical axis), locations/periods with RoU < 0.2 left white). Right: statistical properties (calculated over 1993–2008): time lag at which the flux is most strongly correlated to El Niño (interannually filtered MEI index, Wolter and Timlin, 1993) (upper panel, positive = flux trails MEI), correlation coefficient at this time lag (middle panel), and temporal standard deviation of interannual flux anomalies (lower panel). In the correlation plots, insignificant correlations have been discarded. (The Fig. S4 in Sect. S2 illustrates correlations and time lags again in a time series view.)

BGD
11, 3167–3207, 2014

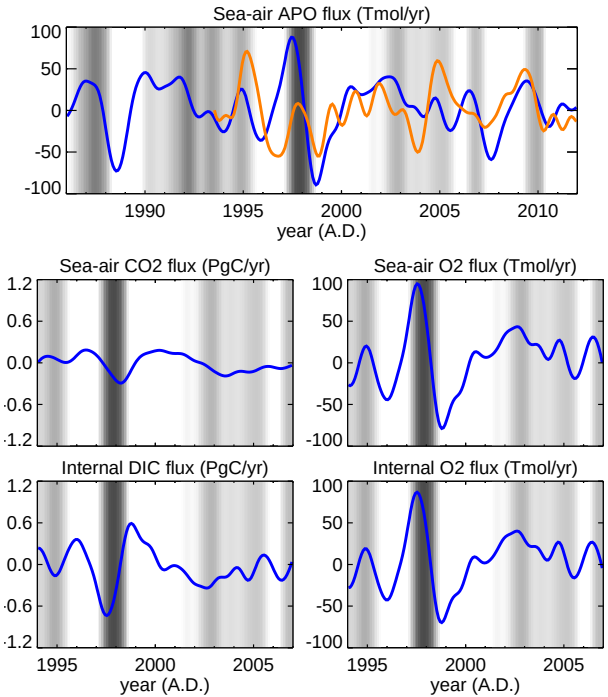

Fig. 7. Top: interannual anomalies of the sea–air flux of atmospheric potential oxygen (APO) in the tropical Pacific, inferred from SOCAT (run *SFC*, blue) or independently estimated from atmospheric O_2/N_2 ratios and CO_2 mixing ratios (atmospheric APO inversion, Rödenbeck et al., 2008, updated, orange). The background shading indicates El Niño (MEI index). Middle: over selected years for illustration, sea–air fluxes of CO_2 and O_2 composing the APO flux (Eq. 5). Bottom: ocean-internal sources and sinks of DIC and O_2. Vertical axes of all panels span the same range on a molar basis.

BGD
11, 3167–3207, 2014

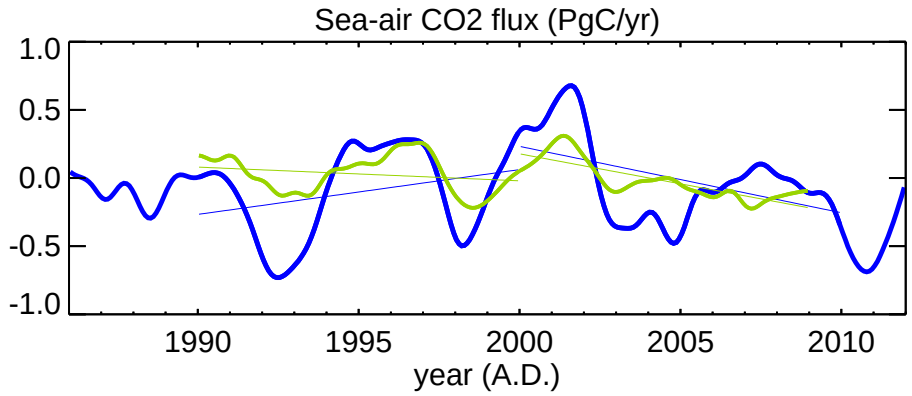

Fig. 8. Interannual anomalies of the total ocean CO_2 flux estimated by run *SFC* (blue) and by the ocean process model run by Buitenhuis et al. (2010) (olive). Linear fits of these results over the 1990–1999 and 2000–2009 periods are overplotted as thin lines.

BGD
11, 3167–3207, 2014

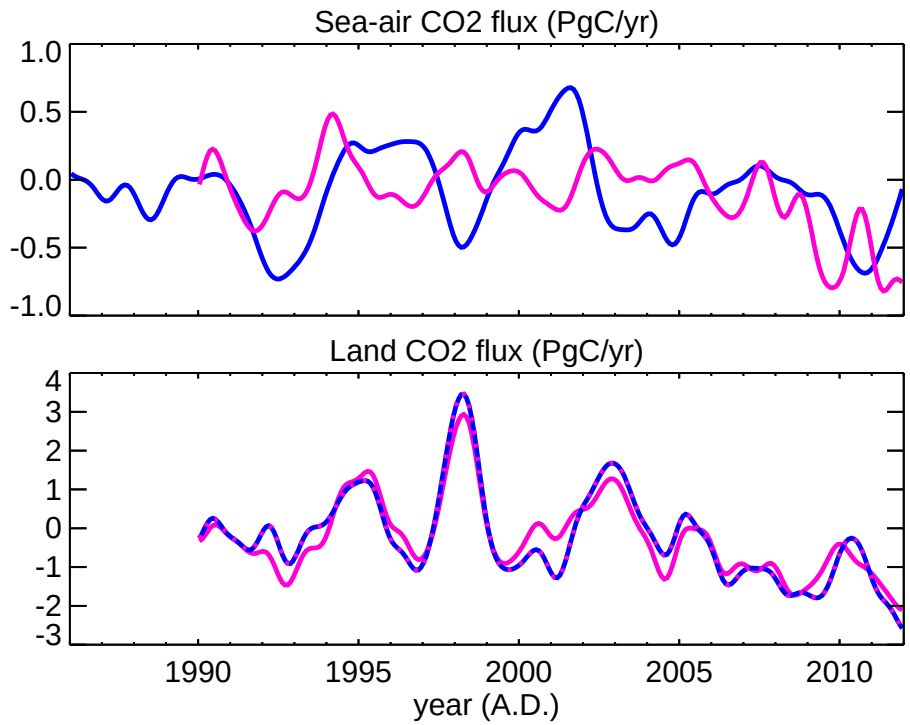

Fig. 9. Top: interannual anomalies of the total ocean CO_2 flux estimated by run *SFC* (blue) and an atmospheric CO_2 inversion (magenta). Bottom: total land CO_2 flux estimated by an atmospheric CO_2 inversion (magenta – standard Jena inversion (s90_v3.5) with constant priors and ocean flux IAV being adjusted from the atmospheric data, dashed magenta/blue – atmospheric inversion using run *SFC* as fixed ocean prior). Note threefold vertical range in the land flux panel relative to ocean panel.

BGD
11, 3167–3207, 2014